Time-resolved imaging of the MALDI linear-TOF ion cloud: Direct visualisation and exploitation of ion optical phenomena using a position and time sensitive detector.

Shane R. Ellis, Jens Soltwisch and Ron M. A. Heeren*

FOM Institute AMOLF, Science Park 104, 1098 XG Amsterdam, The Netherlands

*Corresponding author: heeren@amolf.nl

Abstract

In this study we describe the implementation of a position and time sensitive detection system (Timepix detector) to directly visualise the spatial distributions of the matrix-assisted laser desorption ionization ion cloud in a linear-time-of-flight (MALDI linear-ToF) as it is projected onto the detector surface. These time-resolved images allow direct visualisation of *m/z*-dependent ion focussing effects that occur within the ion source of the instrument. The influence of key parameters, namely extraction voltage (E_V), pulsed-ion extraction (PIE) delay and even the matrix-dependant initial ion velocity was investigated and were found to alter the focussing properties of the ion optical system. Under certain conditions where the spatial focal plane coincides with the detector plane, so-called *x-y* space focussing could be observed (*i.e.*, the focussing of the ion cloud to a small, well defined spot on the detector). Such conditions allow for the stigmatic ion imaging of intact proteins for the first time on a commercial linear ToF-MS system. In combination with the ion optical magnification of the system (~100×), a spatial resolving power of 11-16 μm with a pixel size of 550nm was recorded within a laser spot diameter of ~125 μm. This study demonstrates both the diagnostic and analytical advantages offered by the Timepix detector in ToF-MS

Introduction

Linear time-of-flight mass spectrometry (TOF-MS), in combination with matrix-assisted laser desorption ionization (MALDI), is widely used for the analysis of intact proteins with high (>20,000) mass-to-charge (*m/z*) values. Following the efficiency of the desorption/ionization events of MALDI [1-2], the analytical performance of TOF instruments is largely determined by the ability of the ion-optics to focus the accelerated ions (produced within a two-stage acceleration region) onto the detector that is often located >1 m from the region of ion production. Modern linear TOF instruments employ delayed ion extraction (herein referred to as pulsed-ion extraction (PIE)) to help compensate for the initial velocity spread of produced ions and thus improve mass resolution [3-6]. This aims to ensure that all ions of the same *m/*z are focussed in time and space (along the flight (*z*) axis) within the detector plane. It is in this respect that ion focussing in linear-TOF-MS is often thought of. However, such considerations ignore the ability of the ion optics to ensure ions are simply focussed onto the detector surface (herein referred to as *x*-*y* space focussing, *i.e.* spatial focussing of ions in the detector plane, see **Figure 1**). These spatial focussing abilities largely determine how well the ion image fits the detector (*i.e.,* the fraction of generated ions that are detected), and hence sensitivity. The development of a method to directly visualise such spatial focussing effects in real time in a *m/z*-resolved manner would allow the researcher to optimize and understand how ion source and ion optics influence the ion density reaching the detector. Additionally, it provides a method to image the spatial distribution of the ion cloud as it reaches the detector.

Ion detection in TOF-MS is typically achieved using microchannel plates (MCP) and a single charge collecting anode. However, this approach gives no information pertaining to the impact positions of ions as they reach the detector. To visualise the spatial distribution of ions as they strike the detector surface a position-sensitive detector is required. This capability is

traditionally achieved using an MCP-phosphor screen assembly in combination with a charge-coupled device (CCD) camera [7-8]. However, the long decay time of typical phosphor screens limits their use to either generation of a time-integrated image of all *m/z* values, or an image of a single *m/z* value which requires all other ions be blanked out so they do not contribute to the captured image. As a result time-resolved images of ions with different TOFs cannot be acquired in a single analysis. In addition to the MCP-phosphor screen detector, time and position sensitive ion detection has also been achieved with a variety of alternative approaches including multianode arrays [9-11], wedge and strip anodes [12-13] and delay line detectors [14-16]. However, compared to active pixel detectors [17-18] these approaches may suffer from one or more disadvantages including low spatial resolution due to limited detector density, requirement for time-consuming image reconstruction or the inability to handle the high count rates encountered in MALDI. A comparison of MCP-phosphor screen, delay line and active pixel detectors for mass spectrometry applications is provided in reference [19].

In a recent study [20] we described the implementation of the Timepix active pixel detector [21] on a commercial linear TOF mass spectrometer and presented preliminary data describing how such a position-sensitive detector allows the mass-resolved imaging of the ion cloud. These capabilities stem from the ability of the Timepix detector to record both the impact position and arrival time of individual ion impacts on the detector with excellent signal-to-noise [17]. In this paper we describe in depth the Timepix detector as a useful device for visualisation of ion optical phenomena occurring within the ion source that are essential to instrument performance. Moreover, the ability to visualise these effects in real-time allows for their fast optimisation, exploitation and thereby provides new analytical capabilities for conventional TOF instrumentation.

Experimental Methods

Materials

All solvents, matrices and Immunoglobulin G (IgG, from goat serum) were purchased from Sigma-Aldrich (Zwijndrecht, Netherlands). The protein calibration standard I (consisting of insulin, ubiquitin, cyctochrome C and myoglobin) and protein calibration standard II (consisting of tripsinogen, Protein A and Bovine serum albumin) were purchased from Bruker GmbH (Bremen, Germany) and prepared according to the manufacturer instructions. Sinapinic acid (SA), ferrulic acid (FA) and 2, 6-dihydroxyacetophenone (DHAP) were prepared as 20 $mg.mL^{-1}$ solutions in 1:1 acetonitrile:water (v/v) + 0.1% trifluoroacetic acid (TFA). α-cyano-4-hydroxycinnamic acid (CHCA) was prepared in an analogous manner albeit as a 10 $mg.mL^{-1}$ solution. To produce a more homogenous matrix layer, 2, 5-dihydroxybenzoic acid (DHB) was prepared as an aqueous solution (10 $mg.mL^{-1}$) with the addition of a small amount of glycerol as previously described [22] and allowed to dry under vacuum within the ion source region. Analysis solutions were prepared by mixing either a protein calibration mix or IgG solution 1:1 (v/v) with the matrix solution. 1 µL aliquots of analysis solutions were then deposited onto a stainless steel target plate and air-dried prior to MALDI analysis.

Mass Spectrometry and Ion Detection System

A schematic of the instrumental setup is shown in **Figure 1**. All mass spectrometry experiments were performed on an Ultraflex III MALDI TOF-MS (Bruker Daltonik GmbH, Bremen, Germany) equipped with a Smartbeam® 355 nm Nd:YAG laser system. Experiments were performed with a 25 kV acceleration voltage and a laser frequency of 10 Hz. Control

over extraction and Einzel lens voltages and pulsed-ion extraction (PIE) delay time was achieved via the standard FlexControl 3.0 software (Bruker Daltonik GmbH, Bremen, Germany) and reported values correspond to target values input into the software. Note that for the PIE delay there is an intrinsic offset of ~100 ns between the laser firing and the switching of the PIE box for application of the exaction voltage. This means that despite the PIE delay being set to 0 ns, an extraction delay of ~100 ns exists. For stigmatic imaging experiments an additional UV-grade optical lens (focal length ~ 150 mm) was placed in the laser path behind the telescope optics to provide a larger spot size (~125 µm diameter) that cannot typically be achieved with the UltraflexIII optics.

The Timepix-based [21] detection system employed is identical to that previously described [20, 23] and replaces the conventional linear detector. The detection system is similar to the commercially available IonPix system (Omics2Image BV, Amsterdam, The Netherlands). The detector assembly introduces additional length of ~20 cm to the ion flight path. The Timepix chips each have dimensions of 1.4×1.6 cm^2 and contain an array of 256 x 256 pixels (55 µm pitch) where each pixel is an independent single stop time-to-digital converter (TDC). In this study a 2×2 chip array is used thus providing a 512 x 512 pixel array for ion detection. Each pixel is operated in time-of-arrival mode (*i.e.*, each pixel records the arrival time of an event with respect to the laser pulse that is defined as t = 0). The Timepix clock was operated at 40 MHz (25 ns time bins), that in combination with the counter depth of 11810, provides a maximum measurement window of 295 µs. The trigger signals that determine both start time of the Timepix acquisition windows with respect to the laser pulse and the length of the acquisition window were generated by a pulse and delay generator (DG535, Stanford Research Systems, CA, USA).

The Timepix chip array was mounted 2 mm behind a chevron MCP stack (active area of 4 cm, 12 µm pores and 15 µm pitch). Homemade power supplies were used to supply high

voltage to the MCP plates. The front MCP was held at -1.75 kV and the back held at -400 V (1.35 kV bias). Chip control and data acquisition was achieved using the dedicated "Pixelman" software package [24]. All data analysis and time-to-mass calibration was performed using in house developed software written in MATLAB (Matlab; Mathworks, Natick, MA, USA; ver. 7.13.0.564, R2010b). All images/spectra represent the integration of 200-1000 laser shots.

Results and Discussion

Visualisation of ion focussing and influence of electrode geometry

The time-resolved imaging capabilities of the Timepix detector allows the spatial distribution of a particular component in the MALDI ion cloud to be imaged as it is projected onto the detector surface (the *x-y* plane as depicted in **Figure 1**). The spatial orientation of the ion cloud is dependent on the initial ion velocity distribution as well as the ion-optical effects occurring in the ion source during extraction and acceleration. Within the ion source, the extraction and acceleration regions essentially constitute an electrostatic ion optical lens system followed by an Einzel lens (P_4). The holes in P_2 and P_3 form electrostatic aperture lenses (see **Figures 1 and 2**) [25]. The combined focal length of the ion-optical system is dependent on its design, the voltages applied to the each electrode element, as well the velocity, mass and charge of the ions. Given typical electrostatic lenses posses a focal length that is dependent on the ion energy, we speculate the *m/z* dependence of the focal length may arise from several factors such as mass-dependent kinetic energies arising from the initial ion velocities and the shape of the extraction pulse, in addition to the momentum dependent angular deviation of accelerating electrostatic lens elements [25].

Figure 2a shows the integrated (200 laser shots) ion distribution of doubly charged protein A (*m/z* 22307) the instant it arrives at the detector as a function of extraction voltage (E_V, defined as the voltage drop applied across P_1 and P_2). The Einzel lens was set to 6 kV and a PIE-delay of 500 ns was employed while the ion counts recorded by each pixel (maximum 1 count per pixel per laser shot) are depicted by colour with bright shades indicating high impact rates. Images were acquired with the acquisition of each Timepix frame beginning 120 μs after the laser shot. As each pixel is a single-stop time-to-digital converter, this ensures all

pixels are available to detect the ions interest as they arrive first within the acquisition window. At high E_V values the ion impact position of the few ions that reach the detector are spread over most of the detector surface. By gradually lowering the voltage two effects are observed: (i) a greater number of ions are focussed onto the detector; and (ii) the impact positions are eventually brought into a well-defined focussed spot on the detector surface (at E_V = 2kV). Herein, we refer to these conditions as *x-y* space focussing. *x-y* space focussing conditions are met when the lens equation of the ion optical system ($1/S_1+1/S_2 = 1/f$ with S_1: object distance; S_2 image distance; f: focal length) is met and the image of the *m/z* value investigated lies in the detector plane. As the E_V values are further decreased the ion cloud begins to move out of focus. Defocused images are acquired when the image distance lies either in front (low E_V) or behind (high E_V) the detector surface. Similar focussing effects can be observed with all voltages fixed and varying the PIE delay. This is revealed in **Figure 2b** that was acquired with an E_V of 2.2 kV and an Einzel lens potential of 6 kV. Under these conditions, at 0 ns PIE delay the $[\text{Protein A}]^{2+}$ ions reach the detector completely defocused. With increasing values for the PIE-time the impact region gets smaller and reaches a spatial focus at 900 ns. Increasing PIE times further leads to defocussing. The influence of the PIE-delay can be understood by considering the dependence of the ion focal length on ion energy. With increasing PIE delays the $[\text{Protein A}]^{2+}$ ions drift further away from P_1 towards the extraction electrode (P_2) prior to extraction. Therefore, as the energy gained by an ion during extraction is given by $zE_V[1-(x/d)]$ where x is the distance ions have drifted towards P_2 prior to the application of the extraction field, d is the distance between P_1 and P_2 and z is the charge on the ion, at higher PIE times ions are accelerated to a lower energy that changes the focal length of the system. Ion paths through the system were simulated using the software SIMION 8.0 (Scientific Instrument Services, Ringoes, NJ, USA) for a set of varied extraction voltages, PIE-times and *m/z* values to confirm our experimental observations (Supporting

Information **Figure S1**). For the simulation of different PIE values, the starting point of the ions was shifted towards the first electrode based on an average initial velocity of the ions of 350 m/s [26]. In good agreement with the experimental findings, high E_V, short PIE-time and high *m/z*-values lead to longer focal length and vice versa.

The *m/z* dependence of the focal length was also observed experimentally and is visualised in **Figure 2c** which shows the overlayed, integrated images of $[\text{Protein A}]^{2+}$(*m/z* 22307, shown in red), $[\text{Protein A}]^{1+}$ (*m/z* 44613, shown in green) and $[\text{BSA}]^{1+}$ (*m/z* 66500, shown in blue) acquired at 3 different extraction voltages with a 500 ns PIE-delay. The corresponding mass spectra generated from these data sets are provided as Supporting Information Figure S2. With decreasing E_V ions of higher *m/z* are gradually bought into focus on the detector. With an E_V of 2.4 kV the $[\text{Protein A}]^{2+}$ ions are beginning to move into focus (as evidenced by the cross-like shape), whereas ions of higher *m/z* are defocused. At 2.0 kV E_V $[\text{Protein A}]^{2+}$ is *x*-*y* space focussed onto the detector while the higher *m/*z ions are beginning to move into focus. By contrast, an E_V of 1.8 kV results in the singly charged Protein A being focussed, the doubly charged being beyond focus (as evidenced by the rotated cross) and BSA moving towards focus (upright cross). The ion density that reaches the detector has a large influence on the quality of the spectra. The manner in which this is achieved takes on particular significance with the Timepix due to the single stop TDC nature of the individual pixels and when operating at the high count rates encountered with MALDI. This means that if a pixel is hit by an ion having a particular *m/z*, then this pixel is not available to detect any later arriving ions produced by the same laser shot. This effect is observed in the overlayed image acquired with an E_V of 2.0 kV (**Figure 2c**) that reveals some overlap between the doubly and singly charged Protein A in the centre of the chip (note the lack the singly charged ion (green) detected in the centre). Accordingly, not all of the higher *m/*z ions will be detected due to this overlap. For this reason, the relative intensity of the

singly charged ion to the doubly charged ion is lower than would be recorded with a multi-hit type detector such as a conventional MCP/anode assembly or a multi-hit position-sensitive detector as recently described [18]. These ion count discrepancies are inevitable when there is overlap in the *x*-y ion distributions of different *m/z* values. Nonetheless, the signal-to-noise of the spectra still exceeds that achieved with the conventional integrated MCP/anode detector acquired under identical conditions [20]. **Figure 3** shows a surface plot summarising experimentally determined conditions under which ions of a particular *m/z* are *x-y* space focussed onto the detector. They therefore define a set of parameters producing the same ion optical focal length for the setup. It is apparent, that for any two chosen values, the required focal length for *x*-y space focussing can be achieved by adjusting the third parameter. High E_V values, leading to long focal lengths can be corrected by increasing the *PIE*-time or looking at ions with a lower *m/z*. The same holds true for high *m/z* values producing long focal length that can be compensated by low E_V and/or longer PIE-times. An important parameter in TOF-MS is the velocity-focussing of the ions that influences the mass resolution. Ideally, the ion optics should aim to ensure that the initial velocity distribution of ions of an identical *m/z* is corrected for so the ions arrive at the detector in the narrowest possible time window. However, extraction conditions giving the optimum time focus are not necessarily compatible with spatial focussing conditions [27]. Therefore, while the conditions shown in **Figure 3** allow spatial focussing of ion packets in the *x-y* plane, the temporal spread of the ions arriving at the detector varies according the combination of E_V and PIE-delay used (data not shown).

An interesting feature of the defocused images is the cross-like shape of the ion clouds and its apparent rotation when moving through the focal plane. Depending on the location of the focal plane in front or behind the detector, the orientation of the cross rotates ~45 % (*e.g.*, compare 2.3 kV and 1.8 kV in **Figure 2a**). These effects can be explained by the design of the extraction electrode as shown by the inset in **Figure 2a**. While the ions travel through the

small central bore, the larger holes around it serve for the delivery of the laser beam, lighting and as a camera port. The ion optical properties of the central aperture strongly depend on the electric field structure and in turn on the geometry of the electrode around it. As a result, the presence of four large holes in the electrode distorts the radial uniformity of the extraction field causing the shape of the ion cloud to resemble that of the electrode geometry. This influence of electrode geometry was further investigated with SIMION simulations in an effort to understand the apparent rotation of the cross-like shape observed when the focal plane moves through the detector (see **Figure 2**). **Figure S2** depicts a simulation of the focal length of the two extremes of the electrode geometry as indicated with red and blue bars in the schematic drawing respectively (inset). In the upright cross position (blue bars) only a small metal bar forms the rim of the aperture. In the tilted cross orientation (red bars) the aperture appears to be in a large conductive sheet. As a result of these differences, ions flying through in the horizontal and vertical planes (blue cross) exhibit a longer focal length than their counterparts flying in two corresponding plane tilted 45° (red cross). Therefore, both orientations are focussed onto the detector at slightly different settings with the optimal overall focusing conditions lying somewhere in between. In the case of the focal plane sitting behind the detector, the upright orientation is still slightly less focused than the tilted one and therefore produces a larger radius. The overall picture combines to the upright cross feature (**Figure S2c left**). In the case of the focal plane in front of the detector, the upright orientation is still more focussed than the tilted, leading to an overall tilted cross appearance of the ion distribution (**Figure S2c right**). An alternative P_2 electrode with only three holes surrounding the central bore was implemented to experimentally verify the influence of electrode geometry. (see **inset in Figure 3)**. While the focussing on the detector surface shows the same general dependence on E_V, PIE-time and *m/z*-value, the missing hole on the left side produces

asymmetrical horizontal field distributions leading to distorted ion distributions and no cross-like features (see **Figure 3**).

Different ion cloud distributions are observed with a combination of high E_V, high Einzel lens potential and high *m/z*. Supporting Information **Figure S4a and S4b s**hows the E_V and PIE-delay dependence of ion focussing for singly charged Immunoglobulin G (IgG) ions observed at *m/z* 147,000. **Figure S3a** shows the ion focus dependence on E_V when using an Einzel lens potential of 12 kV a PIE-delay of 500 ns and beginning with an E_V of 5 kV. As the extraction voltage is lowered, IgG ions are observed to be gradually bought into focus. However, interestingly only a faint hint of a cross like shape is observed on the high E_V side of the ion focus. Moving through the detector plane at ~2.6 kV the rotated cross can be observed as the E_V is further decreased. As the PIE-delay is varied using an E_V of 4 kV and an Einzel lens potential of 12 kV (**Figure S4b**), no cross-like shapes are observed but rather with increasing PIE-delay IgG ions are focussed to smaller and smaller circular focus with decreasing ion counts per hit pixel observed above ~2100 ns. Although the origin of these differences was not investigated in detail, we hypothesize it is due to a reduced influence of the first aperture lens (P2) and the higher Einzel lens potential. Focussing under these conditions is achieved with large *m/z* values and high extraction voltages leading to long partial focal lengths from P2 and P3 that are compensated for by the high potential Einzel lens. With these settings most focusing is done by the Einzel lens and only little by the first aperture lens, resulting in less pronounced cross like shapes in the ion distribution on the detector.

Influence of the matrix.

It is well known that the initial axial velocity of desorbed ions produced during MALDI is dependent on the matrix used, and that these matrix-dependent velocities can adversely affect time-to-*m/z* calibration and resolution (time focussing) if not taken into account [26, 28-30]. Given the dependence of the ion focal length on the momentum of the generated ions (see above), we decided to investigate if changes in the initial velocity of ions generated from different matrices yielded observable differences in the *x-y* space focussing conditions for ions with identical *m/z*. **Figure 5** shows ion cloud images of singly charged protein A (MW ~ 45 kDa) acquired from five different matrices with identical ion source conditions (1.5 kV extraction voltage, 0 ns PIE-delay and Einzel lens voltage of 6 kV). Under these conditions ions generated from DHB and DHAP are observed to be well space focussed on the detector. By contrast, ions generated from SA, FA and CHCA matrices produced defocused images on the detector surface, as evidenced by the cross-like shape in the ion cloud distributions. The higher ion intensities observed in the cross-region of SA compared to FA does not necessarily suggest one is more focussed the other, but is simply the result of the higher ion counts observed with SA. Using a lower laser fluence for SA, the distribution looks very similar to that of FA (data not shown). However, the additional "blurriness" observed in the cross region of CHCA suggests it is slightly more defocused then the other matrices. Using axial velocities determined using the delayed extraction approach [26, 29] reported by Glückmann and Karas [26], the order of focussing to defocusing of DHB, SA and CHCA agrees with the reported initial axial velocities of 543 $m.s^{-1}$, 332 $m.s^{-1}$ and 291 $m.s^{-1}$, respectively. However, discrepancies are observed between the focussing order and initial velocities for DHAP and FA, having reported initial velocities of 353 $m.s^{-1}$ and 410 $m.s^{-1}$, respectively. In an effort to understand the potential origin of these discrepancies and to provide evidence the change in ion focussing was due to the initial ion velocity we undertook

our own measurement of the relative axial velocities using the delayed extraction approach. Although the presence of field penetration into the first acceleration region was not investigated, its effect on the high *m/z* ions investigated here would be expected to be minimal [26, 31-32]. In the delayed extraction approach the slope of the linear function plotting TOF against PIE delay is proportional to the initial velocity. These plots are provided as Supporting Information **Figure S5** and provide evidence that DHAP has an initial velocity greater than all matrices except DHB and FA has an initial velocity similar to SA. Using these relative axial velocities the focussing order in Figure 4 becomes consistent with the relative initial axial velocities of the analysed matrices. Although the reasons for axial velocity discrepancies as discussed above are not entirely clear, the FA discrepancy could possibly be caused by the nature of the crystals whereby, at least in our study, FA is observed to from long, thin crystals that rise up off the target plate. It is important to note however, that axial velocity is not the only effect that may influence this analysis. As this data was acquired with the lowest possible delayed extraction time (see methods), ions are accelerated through what is initially a dense plume [33]. Pulling the ions through this dense particle cloud could lead to some potentially matrix dependent loss of energy (and hence velocity) through in-plume collisions [34]. Nonetheless, we believe the initial ion velocities to be the primary source of the matrix-dependent ion focussing effects, although a convolution of this with other plume-related processes cannot be discounted. These observations underline the sensitivity of spatially-resolved ion detection to subtle changes in ion velocity, that in this case, arise via matrix dependent variations in starting velocity.

Exploiting ion focussing effects- Stigmatic imaging with linear-TOF optics

An interesting application of the ion focussing phenomena described above is the ability to acquire an ion optical image of part of the sample surface, *i.e.*, to perform stigmatic ion imaging. Analogous to light microscopy, it would be expected that when a particular *m/z* value is *x*-*y*-space focussed in the detector plane then the spatial distribution with which the ions are observed to strike the detector is representative of their initial distribution on the surface. *i.e.,* a 1-to1 correlation of sample pixel to detector pixel is obtained. This ability, combined with the high *m/z* detection properties of the Timepix [35], would allow high spatial resolution imaging of high *m/z* species independent of the laser spot size. Although "microscope mode" instruments are available (such as the Physical Electronics TRIFT II) [17, 36], these either incorporate dedicated energy-sensitive optics such that all *m/z* values can be focussed and imaged simultaneously, or contain optics similar to those used in this study, but these have both so far been limited to relatively small molecules (<2000 Da) [17-18, 27, 35].

To evaluate the possibility of performing ion microscopy with intact proteins, a protein mix sample was prepared with sinapinic acid and covered with a 37 µm pitch copper transmission-electron microscopy (TEM) grid (**Figure 6a**). The grid served to introduce well-defined structural detail on the surface that would confirm the ability to acquire an ion-optical image representative of the sample surface. To minimise any potential distortion of the initial spatial distributions within the plume following desorption, stigmatic imaging experiments were performed with the lowest possible PIE delay, (PIE delay set to 0 ns in software, see methods) [27]. The doubly charged protein A ions at *m/z* 22307 were chosen for investigation and bought into *x*-*y* space focus using an extraction voltage of 1.68 kV with a 6 kV potential applied to the Einzel lens. **Figure 6b** shows the integrated image on the detector of [Protein A]$^{2+}$ ions acquired following irradiation of a fixed area of the sample with an enlarged (~125 µm) laser beam (1000 shots summed). The grid structure on the surface is clearly reproduced

in the spatial distribution of the [Protein A]$^{2+}$ ions as they strike the MCP surface. As expected desorbed/ionized material originates from the holes within the grid structure. This confirms that *x-y* space focussing has been achieved. The corresponding mass spectra generated during this acquisition showing the signal-to-noise of the measurement (and hence that of the image) is provided as Supporting Information **Figure S6**. The ion optical magnification can be calculated from the average centre-to-centre distance of the high ion count regions in **Figure 6a** that originate from the individual holes in the grid (68 × 55 µm pitch pixels on the detector ≈ 3700 µm) and the known pitch of the TEM grid (36.3 µm). Thus, under these conditions the ion optical magnification is approximately 100×. These data demonstrate for the first time the stigmatic ion imaging of large, high *m/z* proteins. Of course, given the dependence of the focal length on ion *m/z*, under any particular ion source conditions only a narrow *m/z* range will produce an in focus image. **Figures 6 b, c and d** shows the corresponding ion optical images acquired from trypsinogen (*m/z* 23982), doubly charged Protein A (*m/z* 44613) and BSA (*m/z* 66500) in parallel with Protein A^{2+} (see **Figure 6a**). As the *m/z* values increases the ion images get further out of focus as their corresponding focal planes lies further away from detector surface. As a result, distorted images are acquired that do not resemble the initial surface distribution. However, as demonstrated in **Figure 3**, the focal length can adjusted for each *m/z* by varying the ion source conditions and this allows ions with different *m/z* values to be bought into focus when the appropriate *x-y* space focussing conditions are met. The spatial resolving power (herein defined as the distance required for the intensity of a feature to decay from 80% to 20 % of its maximum intensity) has been determined using the pixel intensities measured along the line shown in **Figure 6a**. These intensities are plotted in **Figure 6e** and reveal a resolving power of ~11-16 µm, an order of magnitude greater than the laser spot diameter (~125-130 µm). Previous Timepix studies employing MALDI on dedicated stigmatic imaging instrumentation have

demonstrated resolving powers of 6 µm for peptides [35]. Although the resolving power demonstrated here is 2-3-fold lower than previous values, it has been achieved using proteins at significantly higher *m/z* values and with ion optics not designed/intended to perform stigmatic ion imaging. Inhomogeneities in the pixel intensities arising from different grid positions can adversely affect the calculated spatial resolving power (for example the shallow leading edge for the far right grid position shown in **Figure 6e**). These may be explained by a combination of: (i), some distortion of the ions within the initial plume as instantaneous extraction is not possible (see methods), (ii) the possible presence of some protein/matrix on the top of the grid; (iii) minor ion optical-induced distortions that may arise due to the different focal lengths of ions depending on the position in which the ions travel through the extraction electrode; (iv) possible inhomogeneities in the analyte/matrix distributions on the surface; and (v) the high chemical background detected when analysing the copper grid (see spectra shown in Supporting Information, **Figure S6**). Nonetheless, the demonstrated ability to acquire high contrast stigmatic ion images of intact proteins with a high spatial resolution highlights the high analytical potential in MALDI-TOF-MS.

Conclusions

The use of a Timepix detector enables the acquisition of *m/z*-resolved images of the spatial distribution of the MALDI-linear-TOF ion cloud as it is projected onto the detector. In addition to allowing visualising of ion focussing phenomena as a function of lens voltages, PIE-time, *m/z* value and initial ion velocity, such visualisation capabilities demonstrate that with appropriate *x*-y spatial focussing of the ions onto the detector stigmatic imaging of large intact proteins is achievable. Importantly, such capabilities can be met using commercial linear-TOF instrumentation and can help accelerate the field of microscope mode imaging mass spectrometry for biomolecular analysis. In addition, this approach to ion detection could serve instrument developers as a valuable tool to optimize ion optical design in mass spectrometers, providing a fast and simple method to test new ion optics and to compare ion optical simulations to experimental data. Moreover, due to the sensitivity of ion focussing on electrode potentials we have found such a detection system to be a useful tool for monitoring power supply stability (data not shown). In conclusion, this work demonstrates both the diagnostic capabilities of the Timepix detector and how such a detector can extend the analytical capabilities of ToF-MS for the detection and imaging of high *m/z* (>20,000) species.

Acknowledgments

Part of this research is supported by the Dutch Technology Foundation STW, which is the Applied Science Division of NWO, and the Technology Programme of the Ministry of Economic Affairs, Project OTP 11956. This work is part of the research program of the "Stichting voor Fundamenteel Onderzoek der Materie (FOM)", which is financially supported by the "Nederlandse organisatie voor Wetenschappelijk Onderzoek (NWO)". J.S was supported by a fellowship within the Postdoc Programme of the German Academic Exchange

Service (DAAD). The authors are also grateful to Jens Hoehndorf (Bruker Daltonik GmbH, Bremen, Germany) for his interest and insight into this study and for supplying the alternative extraction electrode and also to Prof. Piet Kistemaker for valuable discussions.

Figure Captions

Figure 1. Schematic of the ion optics and detection system for the linear-TOF instrument used. The coordinate system is defined with the *z*-axis along the flight axis and the detector plane lying in the *x*-*y* plane. Note the schematic is not to scale.

Figure 2. (a) Ion cloud images of [Protein A]$^{2+}$ (*m/z* 22307) acquired by varying the extraction voltage with an Einzel lens voltage of 6 kV and 500 ns PIE-delay. (b) Ion cloud images of [Protein A]$^{2+}$ (*m/z* 22307) acquired by varying the PIE-delay using with an Einzel lens voltage of 6 kV and an extraction voltage of 2.2 kV. The ion counts recorded by each pixel are shown in the scale bar. The extraction electrode is shown as an inset of (a). (c) Overlayed ion cloud images of [Protein A]$^{2+}$ (*m/z* 22307, red), [Protein A]$^{1+}$ (*m/z* 44613, green) and [BSA]$^{1+}$ (*m/z* 66500, blue) acquired using extraction voltages of 2.4 kV, 2.0 kV and 1.8 kV with an Einzel lens voltage of 6 kV and 500 ns PIE-delay. All images are integrated from 200 laser shots.

Figure 3. 3-D surface plot showing conditions under which ions of a particular *m/z* are *x*-*y* space focussed onto the detector.

Figure 4. Ion cloud images of [Protein A]$^{2+}$ (*m/z* 22307) acquired using the alternative extraction electrode with only 3 outer holes by varying the extraction voltage with an Einzel lens voltage of 6 kV and 500 ns PIE-delay. The extraction electrode is shown in the inset. he ion counts recorded by each pixel are shown in the scale bar. (b) Overlayed ion cloud images

of [Protein A]$^{2+}$ (*m/z* 22307, red), [Protein A]$^{1+}$ (*m/z* 44613, green) and [BSA]$^{1+}$ (*m/z* 66500, blue) acquired with the alternate electrode using extraction voltages of 2.4 kV, 2.2 kV and 1.9 kV with an Einzel lens voltage of 6 kV and 500 ns PIE-delay.

Figure 5. Ion cloud images of singly charged Protein A (*m/z* 44613) produced from (a) 2, 5-dihydroxybenzoic acid (DHB), (b) 2, 6-dihydroxyacetophenone (DHAP), (c) sinapinic acid (SA), (d) ferrulic acid (FA) and (e) α-cyano-4-hydroxycinnamic acid (CHCA). All images represent the sum of 500 laser shots and were acquired with an extraction voltage of 1.5 kV, 0 ns PIE-delay and an Einzel lens voltage of 6 kV. Absolute ion counts recorded by each pixel are shown in the corresponding scale bars.

Figure 6. (a) Stigmatic ion image of [Protein A]$^{2+}$ (*m/z* 22307) acquired by covering the sample with a 37 μm pitch transition electron microscopy grid (see inset). The approximate laser spot size is indicated on the grids image shown in the inset. Image was acquired by summing 1000 laser shots using an extraction voltage of 1.68 kV, Einzel lens 6 kV and no PIE delay. Corresponding images showing the ion cloud images of (b) [Trypsinogen]$^{1+}$ (*m/z* 23982), (c) [Protein A]$^{1+}$ (*m/z* 44613) and (d) [BSA]$^{1+}$ (*m/z* 66500) acquired in parallel as (a). Ion clouds recorded by each pixel are indicated in the corresponding colour scale bars. (e) Determination of the spatial resolving power of the stigmatic image in (a) by plotting the ion counts recorded across the line shown in red in (a).

Figures

Figure1

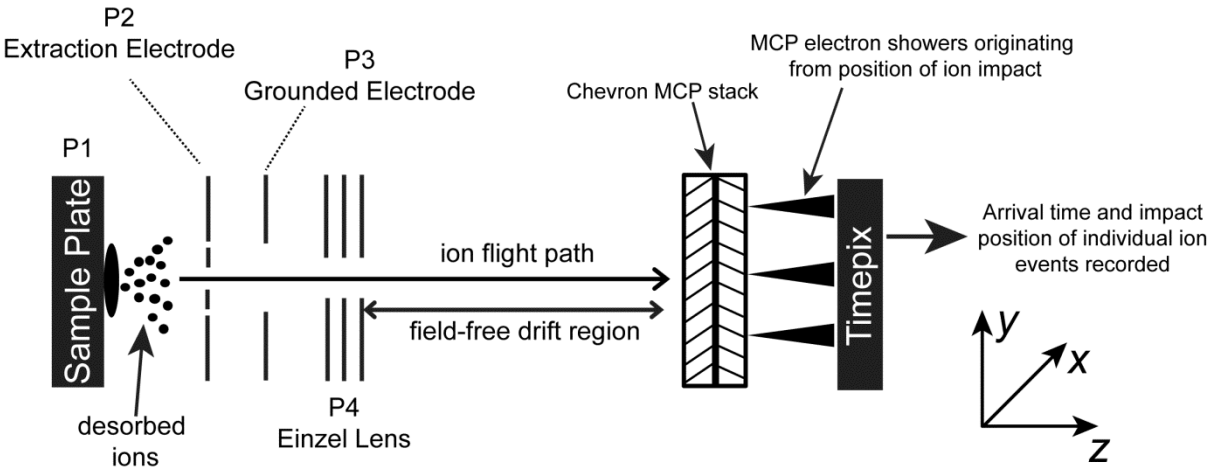

Figure 2

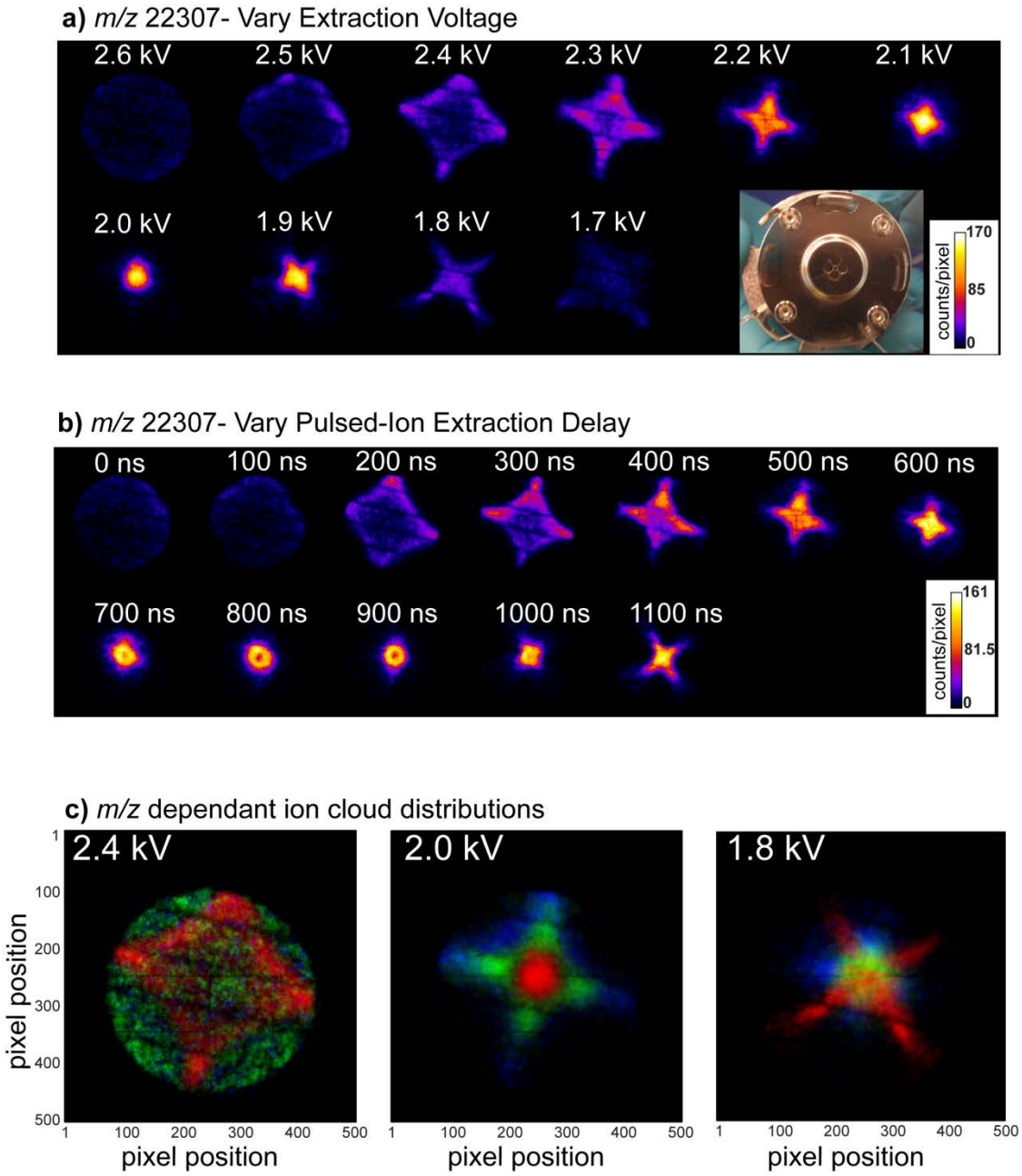
a) m/z 22307- Vary Extraction Voltage
2.6 kV
2.5 kV
2.4 kV
2.3 kV
2.2 kV
2.1 kV
2.0 kV
1.9 kV
1.8 kV
1.7 kV
counts/pixel
170
85
0
b) m/z 22307- Vary Pulsed-Ion Extraction Delay
0 ns
100 ns
200 ns
300 ns
400 ns
500 ns
600 ns
700 ns
800 ns
900 ns
1000 ns
1100 ns
counts/pixel
161
81.5
0
c) m/z dependant ion cloud distributions
2.4 kV
2.0 kV
1.8 kV
pixel position
pixel position
pixel position
pixel position
1
100
200
300
400
500

Figure 3

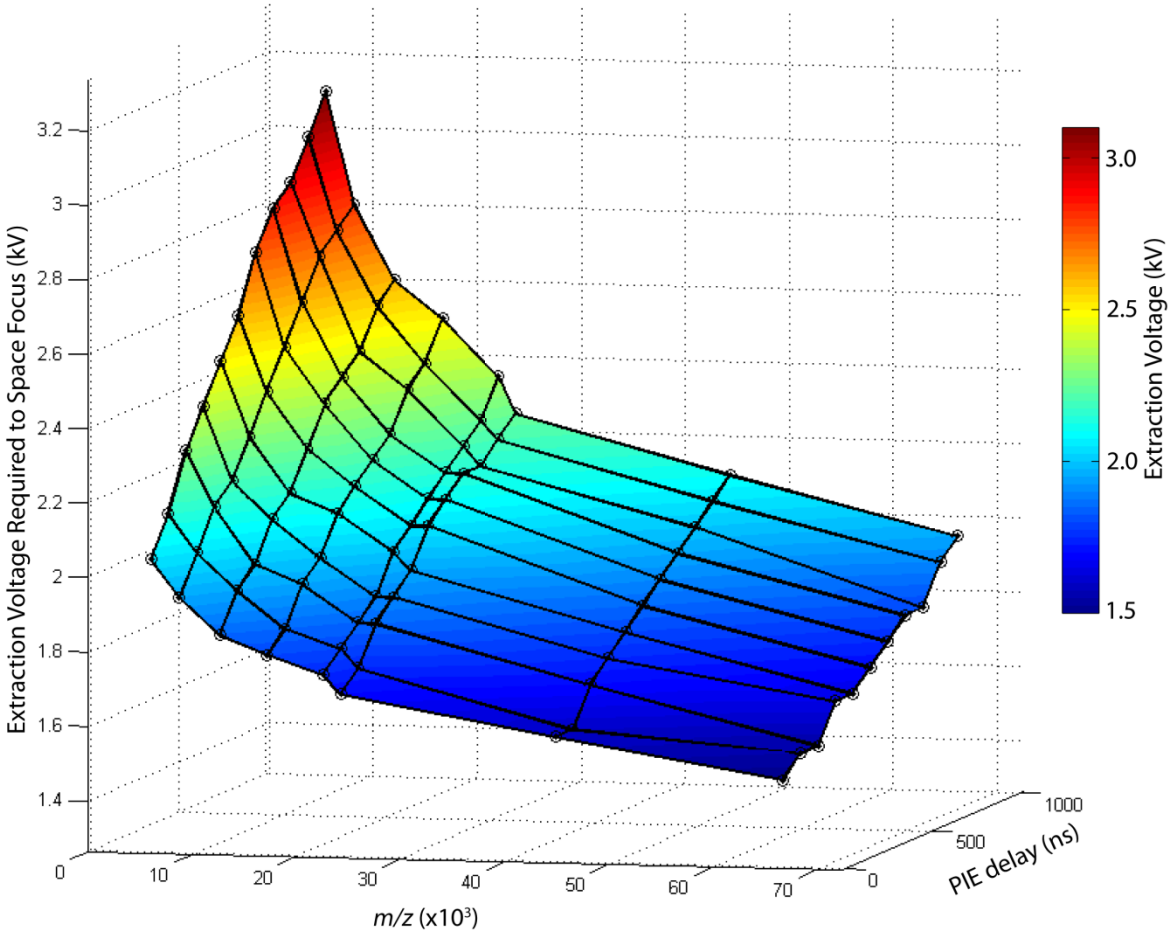
Extraction Voltage Required to Space Focus (kV)
3.2
3
2.8
2.6
2.4
2.2
2
1.8
1.6
1.4
0
10
20
30
40
50
60
70
m/z (x10³)
0
500
1000
PIE delay (ns)
3.0
2.5
2.0
1.5
Extraction Voltage (kV)

Figure 4

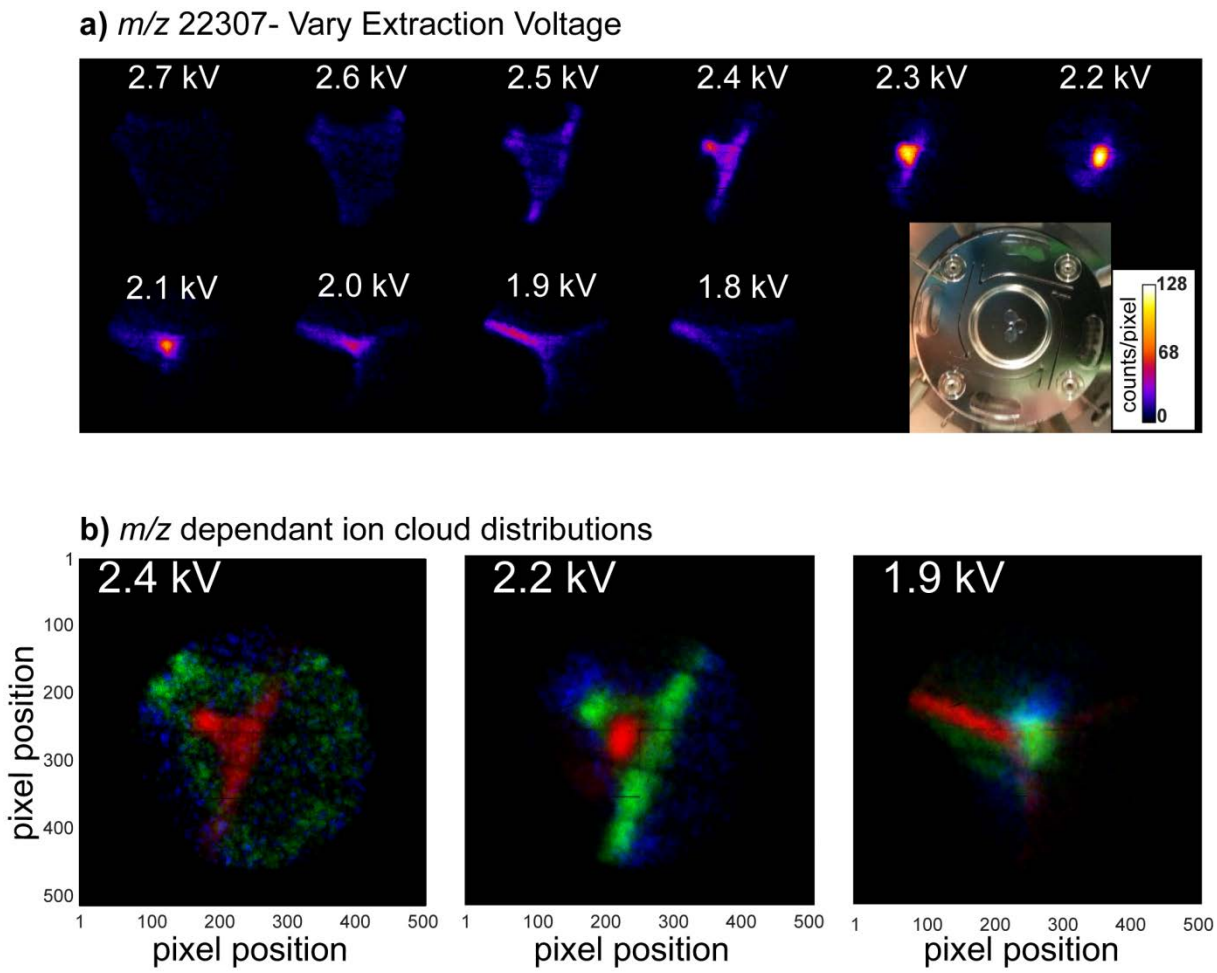
a) m/z 22307- Vary Extraction Voltage
2.7 kV
2.6 kV
2.5 kV
2.4 kV
2.3 kV
2.2 kV
2.1 kV
2.0 kV
1.9 kV
1.8 kV
counts/pixel
128
68
0
b) m/z dependant ion cloud distributions
2.4 kV
2.2 kV
1.9 kV
pixel position
1
100
200
300
400
500

Figure 5.

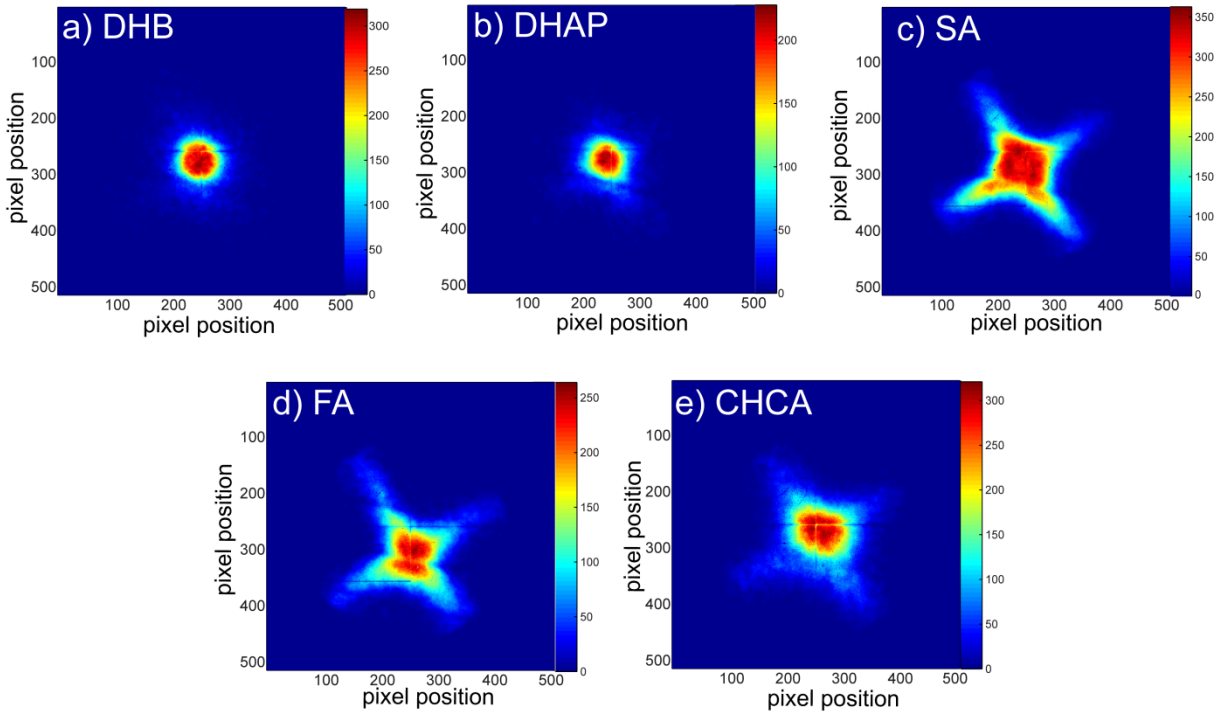

Figure 6

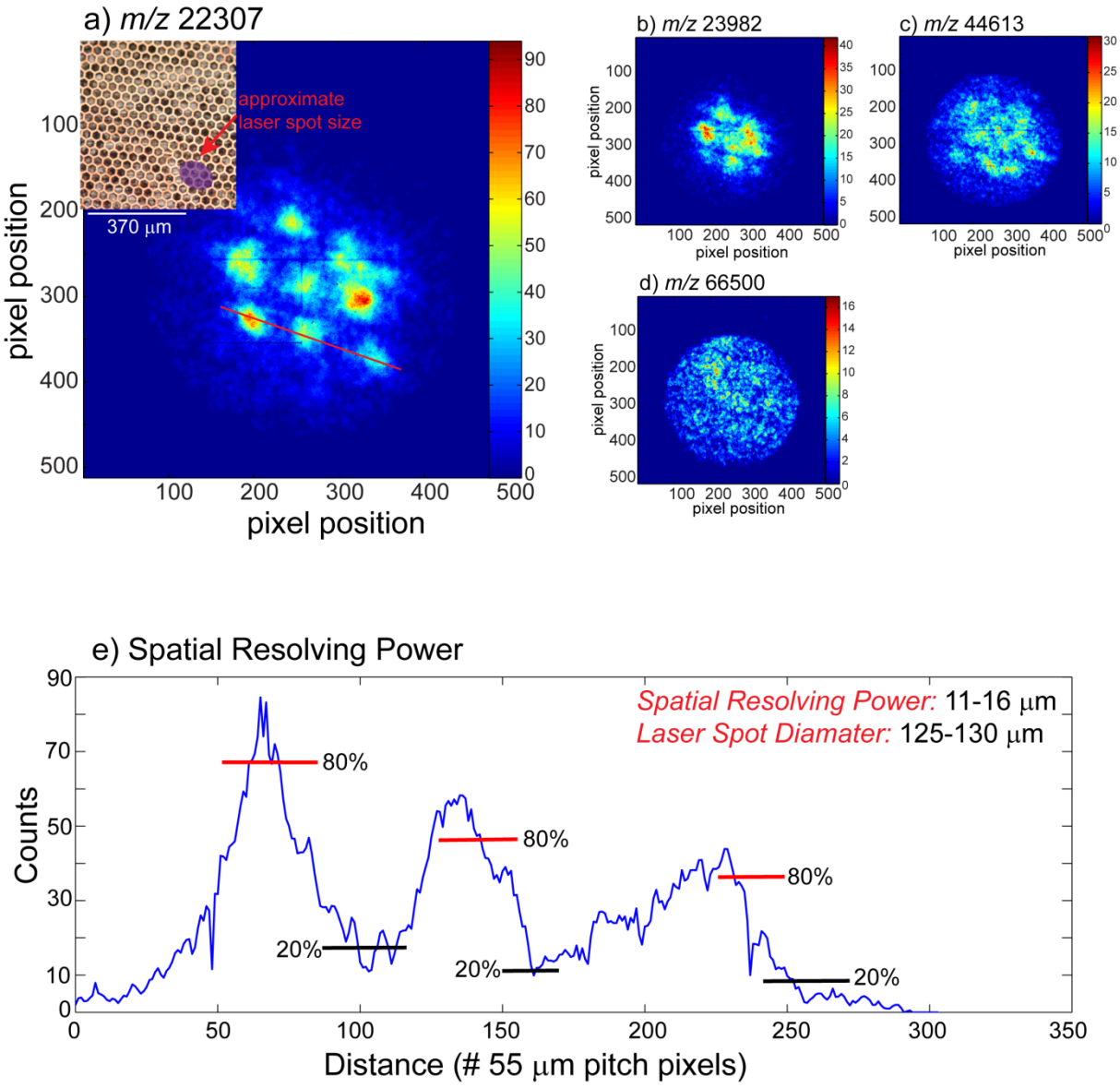
a) m/z 22307
approximate
laser spot size
370 μm
pixel position
pixel position
b) m/z 23982
pixel position
pixel position
c) m/z 44613
pixel position
pixel position
d) m/z 66500
pixel position
pixel position
e) Spatial Resolving Power
Spatial Resolving Power: 11-16 μm
Laser Spot Diamater: 125-130 μm
80%
80%
80%
20%
20%
20%
Counts
Distance (# 55 μm pitch pixels)

References

(1) Dreisewerd, K., The desorption process in MALDI. *Chem. Rev.* **2003**, *103*, 395-426.
(2) Knochenmuss, R., Ion formation mechanisms in UV-MALDI. *Analyst* **2006**, *131*, 966-986.
(3) Colby, S. M., Reilly, J. P., Space−velocity correlation focusing. *Anal. Chem.* **1996**, *68*, 1419-1428.
(4) King, T. B., Colby, S. M., Reilly, J. P., High resolution MALDI-TOF mass spectra of three proteins obtained using space—velocity correlation focusing. *Int. J. Mass. Spectrom. Ion Procces.* **1995**, *145*, L1-L7.
(5) Wiley, W. C., McLaren, I. H., Time-of-flight mass spectrometer with improved resolution. *Rev. Sci. Instrum.* **1955**, *26*, 1150-1157.
(6) Spengler, B., Cotter, R. J., Ultraviolet laser desorption/ionization mass spectrometry of proteins above 100,000 daltons by pulsed ion extraction time-of-flight analysis. *Anal. Chem.* **1990**, *62*, 793-796.
(7) Luxembourg, S. L., Mize, T. H., McDonnell, L. A., Heeren, R. M. A., High-spatial resolution mass spectrometric imaging of peptide and protein distributions on a surface. *Anal. Chem.* **2004**, *76*, 5339-5344.
(8) Hazama, H., Aoki, J., Nagao, H., Suzuki, R., Tashima, T., Fujii, K.-i., Masuda, K., Awazu, K., Toyoda, M., Naito, Y., Construction of a novel stigmatic MALDI imaging mass spectrometer. *Appl. Surf. Sci.* **2008**, *255*, 1257-1263.
(9) Pollard, J. E., Lichtin, D. A., Janson, S. W., Cohen, R. B., Time-resolved mass and energy analysis by position-sensitive time-of-flight detection. *Rev. Sci. Instrum.* **1989**, *60*, 3171-3180.
(10) Bouneau, S., Cohen, P., Della Negra, S., Jacquet, D., Le Beyec, Y., Le Bris, J., Pautrat, M., Sellem, R., 256-anode channel plate device for simultaneous ion detection in time of flight measurements. *Rev. Sci. Instrum.* **2003**, *74*, 57-67.
(11) Della-Negra, S., Depauw, J., Guillermier, C., Schweikert, E. A., Massive clusters: Secondary emission from qkeV to qMeV. New emission processes? New SIMS probe? *Surf. Interface Anal.* **2011**, *43*, 62-65.
(12) Cerezo, A., Godfrey, T. J., Smith, G. D. W., Application of a position-sensitive detector to atom probe microanalysis. *Rev. Sci. Instrum.* **1988**, *59*, 862-866.
(13) Martin, C., Jelinsky, P., Lampton, M., Malina, R. F., Anger, H. O., Wedge-and-strip anodes for centroid-finding position-sensitive photon and particle detectors. *Rev. Sci. Instrum.* **1981**, *52*, 1067-1074.
(14) Klerk, L. A., Lockyer, N. P., Kharchenko, A., MacAleese, L., Dankers, P. Y. W., Vickerman, J. C., Heeren, R. M. A., C60+ secondary ion microscopy using a delay line detector. *Anal. Chem.* **2009**, *82*, 801-807.
(15) Froesch, M., Luxembourg, S., Verheijde, D., Heeren, R., Imaging mass spectrometry using a delay-line detector. *Eur. J. Mass Spectrom.* **2010**, *16*, 35-45.
(16) Jagutzki, O., Cerezo, A., Czasch, A., Dorner, R., Hattas, M., Min, H., Mergel, V., Spillmann, U., Ullmann-Pfleger, K., Weber, T., Schmidt-Bocking, H., Smith, G. D. W., Multiple hit readout of a microchannel plate detector with a three-layer delay-line anode. *IEEE. Trans. Nucl. Sci.* **2002**, *49*, 2477-2483.

(17) Jungmann, J. H., MacAleese, L., Visser, J., Vrakking, M. J. J., Heeren, R. M. A., High dynamic range bio-molecular ion microscopy with the timepix detector. *Anal. Chem.* **2011**, *83*, 7888-7894.
(18) Brouard, M., Halford, E., Lauer, A., Slater, C. S., Winter, B., Yuen, W. H., John, J. J., Hill, L., Nomerotski, A., Clark, A., Crooks, J., Sedgwick, I., Turchetta, R., Lee, J. W. L., Vallance, C., Wilman, E., The application of the fast, multi-hit, pixel imaging mass spectrometry sensor to spatial imaging mass spectrometry. *Rev. Sci. Instrum.* **2012**, *83*, 114101-114109.
(19) Jungmann, J. H., Heeren, R. M. A., Emerging technologies in mass spectrometry imaging. *J. Proteomics* **2012**, *75*, 5077-5092.
(20) Ellis, S. R., Jungmann, J. H., Smith, D. F., Soltwisch, J., Heeren, R. M. A., Enhanced detection of high-mass proteins by using an active pixel detector. *Angew. Chem. Int. Ed.* **2013**, *52*, 11261-11264.
(21) Llopart, X., Ballabriga, R., Campbell, M., Tlustos, L., Wong, W., Timepix, a 65k programmable pixel readout chip for arrival time, energy and/or photon counting measurements. *Nucl. Instrum. Methods. Phys. Res. A* **2007**, *581*, 485-494.
(22) Soltwisch, J., Berkenkamp, S., Dreisewerd, K., A binary matrix of 2,5-dihydroxybenzoic acid and glycerol produces homogenous sample preparations for matrix-assisted laser desorption/ionization mass spectrometry. *Rapid Commun. Mass Spectrom.* **2008**, *22*, 59-66.
(23) Kiss, A., Jungmann, J. H., Smith, D. F., Heeren, R. M. A., Microscope mode secondary ion mass spectrometry imaging with a timepix detector. *Rev. Sci. Instrum.* **2013**, *84*, 013704-013707.
(24) Turecek, D., Holy, T., Jakubek, J., Pospisil, S., Vykydal, Z., Pixelman: A multi-platform data acquisition and processing software package for medipix2, timepix and medipix3 detectors. *J. Instrum.* **2011**, *6*, C01046.
(25) Hinterberger, F., in *CERN Accelerator School and KVI: Specialised CAS Course on Small Accelerators*, ed. D. Brandt. Zeegse, The Netherlands, 2006.
(26) Glückmann, M., Karas, M., The initial ion velocity and its dependence on matrix, analyte and preparation method in ultraviolet matrix-assisted laser desorption/ionization. *J. Mass Spectrom.* **1999**, *34*, 467-477.
(27) Aoki, J., Hazama, H., Yoyoda, M., Novel ion extraction method for imaging mass spectrometry. *J. Mass Spectrom. Soc. Jpn.* **2011**, *59*, 57-61.
(28) Karas, M., Bahr, U., Fournier, I., Glückmann, M., Pfenninger, A., The initial-ion velocity as a marker for different desorption-ionization mechanisms in MALDI. *Int. J. Mass. Spectrom.* **2003**, *226*, 239-248.
(29) Juhasz, P., Vestal, M., Martin, S., On the initial velocity of ions generated by matrix-assisted laser desorption ionization and its effect on the calibration of delayed extraction time-of-flight mass spectra. *J. Am. Soc. Mass. Spectrom.* **1997**, *8*, 209-217.
(30) Costa Vera, C., Zubarev, R., Ehring, H., Hakansson, P., Sunqvist, B. U. R., A three-point calibration procedure for matrix-assisted laser desorption/ionization mass spectrometry utilizing multiply charged ions and their mean initial velocities. *Rapid Commun. Mass Spectrom.* **1996**, *10*, 1429-1432.
(31) Schürenberg, M., Schulz, T., Dreisewerd, K., Hillenkamp, F., Matrix-assisted laser desorption/ionization in transmission geometry: Instrumental implementation and mechanistic implications. *Rapid Commun. Mass Spectrom.* **1996**, *10*, 1873-1880.
(32) Berkenkamp, S., Menzel, C., Hillenkamp, F., Dreisewerd, K., Measurements of mean initial velocities of analyte and matrix ions in infrared matrix-assisted laser desorption ionization mass spectrometry. *J. Am. Soc. Mass. Spectrom.* **2002**, *13*, 209-220.

(33) Vertes, A., Irinyi, G., Gijbels, R., Hydrodynamic model of matrix-assisted laser desorption mass spectrometry. *Anal. Chem.* **1993**, *65*, 2389-2393.
(34) Zhou, J., Ens, W., Standing, K. G., Verentchikov, A., Sundqvist, B. U. R., Kinetic energy measurements of molecular ions ejected into an electric field by matrix-assisted laser desorption. *Rapid Commun. Mass Spectrom.* **1992**, *6*, 671-678.
(35) Jungmann, J., Smith, D., MacAleese, L., Klinkert, I., Visser, J., Heeren, R., Biological tissue imaging with a position and time sensitive pixelated detector. *J. Am. Soc. Mass. Spectrom.* **2012**, *23*, 1679-1688.
(36) Luxembourg, S. L., McDonnell, L. A., Mize, T. H., Heeren, R. M. A., Infrared mass spectrometric imaging below the diffraction limit. *J. Proteome Res.* **2005**, *4*, 671-673.